RSC Advances

PAPER

View Article Online
View Journal | View Issue

Cite this: *RSC Adv.*, 2022, **12**, 26245

Bi-functional water-purification materials derived from natural wood modified TiO_2 by photothermal effect and photocatalysis†

Hui Zhang,[a] Xiaohua Wang,[b] Yao Wang,[a] Zhizhi Gu*[c] and Liyong Chen *[ab]

As one of the sustainable and renewable materials, the carbonization of natural wood is generally considered as a low-cost, environmentally friendly method to fabricate carbon materials. Natural wood, by surficial carbonization, can possess an excellent photothermal effect, low heat loss, and easy water transportation in the solar water desalination process based on the unique structures, leading to high solar water desalination performance. Here, we design and construct a composite of commercial P25 nanocrystal-loaded semi-spherical wood with surficial carbonization at the semi-spherical end (P25/wC-s-s), which is beneficial for light harvesting and water evaporation due to the semi-spherical structure-induced large surface area. The composite displays bi-functions of high solar-to-vapour energy efficiency and an intriguing photo-degradation efficiency for organic pollutants in the solar water purification process. The research provides a novel approach to engineering an efficient, stable, and low-cost bi-functional device for the photothermal/photoelectronic conversion of water treatment.

Received 29th March 2022
Accepted 30th August 2022

DOI: 10.1039/d2ra02013k

rsc.li/rsc-advances

Introduction

Recently, the shortage of water resources is becoming increasingly serious, caused by increased population and human activity-related water contamination.[1–3] The large-scale use of aromatic organic compounds in industry, modern agriculture, and our daily life is the main origin of organic pollutants in natural water.[4,5] Hence, to address the global water issue, on the one hand, it is needed to build awareness of water conservation and reduce pollution emission, and on the other hand, the development of new technologies for the removal of these pollutants from impaired water and harvesting clean water from natural water.[4,6–8] Photo-degradation of organic pollutants by various inorganic semiconductor nanocrystals or enrichment of hazardous pollutants using porous materials with specific surface area as adsorbents in water treatment has been considered as an effective strategy for water purification.[9–18] In addition, the solar water generation technology, utilizing solar energy to evaporate water from polluted water or seawater, has been widely explored in the field of water engineering to obtain fresh water.[19–22] In combination with these processes, the aforementioned technologies could play a more effective role in dealing with the shortage of water resources and improve the environment of the global water system. Following this idea, an ingenious framework involving the integration of solar-thermal conversion, photocatalytic degradation, and physical adsorption as well into a composite is proposed in the research.

The light absorption ability of photothermal materials is determined by their intrinsic properties and also affected by the surface area and the optical path length.[23] As one of the most promising photothermal materials, carbon has been intensely studied in the solar-thermal desalination of seawater due to its strong light absorption ability in the range of the full spectrum.[24–26] In contrast to other precursors for the preparation of carbon materials, natural wood has abundant porous structures related to aligned channels inducing the long optical path length, beneficial for the light absorption and water transportation and evaporation on the top of wood carbon by capillary force.[19,27–30] Hence, to immensely boost the solar water generation performance, the wood carbon was used as a solar absorber by the carbonization of natural wood with semi-spherical structures to maximize surface area for the enhancement of solar energy harvesting based on the interaction of much more carbons with photons. Some pioneering research works on the surficial carbonization of wood provided a feasible solution to lower heat loss to the environment and keep the absorption capability of solar energy in the process of solar water evaporation.[19,27,31,32] Herein, a tree-inspired material, white oak block that was manufactured in a semi-spherical shape at one end, was used as a precursor to prepare porous

[a]State Key Laboratory of Fine Chemicals, Dalian University of Technology, Dalian 116024, China. E-mail: lychen@dlut.edu.cn

[b]Department of Pharmaceutical Engineering, Bengbu Medical College, Bengbu, 233030, China

[c]College of Fisheries and Life Science, Dalian Ocean University, Dalian 116023, China. E-mail: guzhizhi@dlou.edu.cn

† Electronic supplementary information (ESI) available: Experimental procedures, XRD patterns, SEM images, Raman spectrum, solar water generation performance, and RhB photo-degradation. See https://doi.org/10.1039/d2ra02013k

wood carbon by the surficial carbonization of the semi-spherical end (defined as wC-s-s); and P25-based nanomaterials that have been broadly employed as photocatalysts for the degradation of organic pollutants were immobilized on the surface of wood without carbonization.[33–35] Finally, the composite P25 loaded wC-s-s (defined as P25/wC-s-s) was used to study the solar water evaporation and photo-degradation of organic pollutant rhodamine B (RhB) from the polluted seawater.

Results and discussion

Morphology, microstructure, and textural property

The natural wood of white oak was processed into small blocks of 3 cm in diameter and 2.5 cm in height along its growth direction. One end of a small wood block was polished to form a semi-spherical shape (Fig. 1a, left). Afterwards, the semi-spherical end was placed on a conventional hot plate with a heating mantle that was filled with quartz sand to uniformly carbonize the semi-spherical end at a controllable temperature of 400 °C to produce the heterostructures of surficially carbonized wood blocks (Fig. 1a, medium). The carbonized thickness of wC-s-s can be adjusted by the carbonization time, and the carbon layer of wC-s-s is around 0.6 cm in thickness if a wood block is thermally treated for 25 min (wC-s-s-25) (Fig. S1†). Commercial P25 nanocrystals with diameters of ~50 nm were sonicated in ethanol to form uniform suspensions and loaded on the surface of wC-s-s-25 to achieve the P25/wC-s-s-25 composites by a simple drop-casting method (Fig. 1a, right). The scanning electron microscopy (SEM) image (Fig. 1b) revealed that a large number of pores with diameters of ~20 μm were identified from the carbonized surfaces of wC-s-s, originating from vessels and fibre tracheids of cellular structures (Fig. S2†). These aligned pores grow along the vertical direction to form transport channels that were not damaged after carbonization (Fig. 1c). P25 nanocrystal (Fig. S3†) loaded wC-s-s-25 were successfully prepared and confirmed by SEM image showing many white aggregates (Fig. 1d) and X-ray diffraction (XRD) pattern (Fig. S4†). The Raman spectrum of P25 peaked at 144, 197, 396, 515, and 638 cm^{-1}, corresponding to the Raman shifting of anatase TiO_2, and 144 and 445 cm^{-1} assigned to the E_g modes of rutile TiO_2 can be observed from that of P25/wC-s-s-25,[36,37] further suggesting the formation of the composite (Fig. S5†).

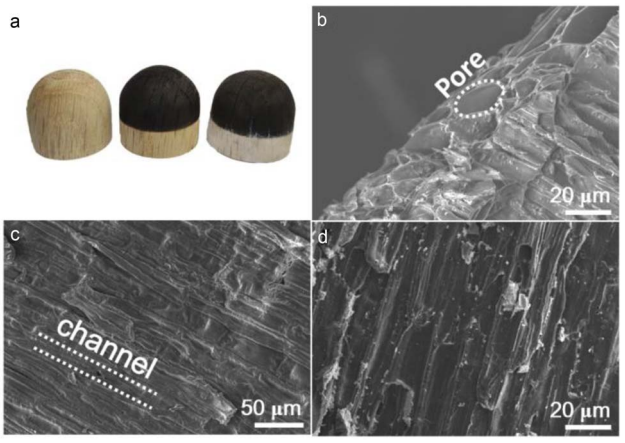

Fig. 1 (a) Optical photograph of the wood block with semi-spherical shape at one end, wC-s-s-25, and P25/wC-s-s-25 (from left to right); SEM images of (b) porous structures of wC-s-s-25 from top view, (c) well aligned channels of wC-s-s-25 from the cross-section, and (d) P25/wC-s-s-25.

Optical property and photothermal effect

The light absorption ability of photothermal materials serves as a key factor in determining their performance for solar water generation. Porous microstructures of wC-s-s-25 play an important role in enhancing the absorption by elongating the optical path.[19,38] The UV-Vis-NIR spectrum of wC-s-s was measured and showed strong light harvesting behaviour throughout the whole solar spectrum ranging from 350 to 2000 nm (Fig. 2a, black), particularly from 350 to 1000 nm, in which solar energy is concentrated (Fig. 2a, red). The absorbance of wC-s-s-25 is much higher than that of natural wood (Fig. 2a, wine). Hence, the superior light absorption ability of wC-s-s-25 is dominantly attributed to the surficial carbonization of natural woods.

After loading P25 nanocrystals on the surfaces of the carbon domain, the as-formed composites show a similar absorption spectrum to wC-s-s-25 (Fig. 2a, blue), revealing that P25 nanocrystals do not affect the light absorption ability of black carbons. On these bases, P25 nanocrystals with relatively low light absorption ability within the whole solar spectrum range should preferentially be immobilized on the surfaces of wood domains to achieve the photo-degradation of organic pollutants by minimizing the impact of carbons on the light shield. Predictably, the separated structures of photothermal materials and photocatalysts are beneficial for solar-thermal conversion and photo-degradation performance.

To intuitively understand the photothermal effect, IR imaging was conducted to monitor the temperature change of wC-s-s-25 upon light irradiation. Fig. 2b shows the temperature of wC-s-s-25 rises from 31.1 °C to 47.2 °C under simulated sunlight irradiation (1 kW m^{-2}) for 1 min, and the highest temperature can reach 61.8 °C within 5 min. Furthermore, the photothermal effect of wC-s-s-25 floating on water was studied. Under the conditions, wC-s-s-25 displayed a similar

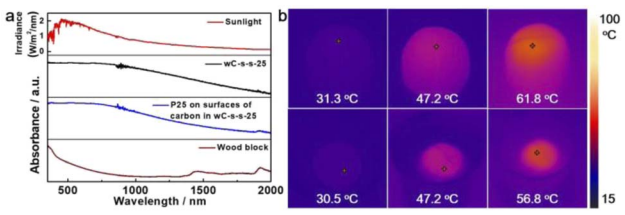

Fig. 2 (a) Spectrum of sunlight, and UV-visible absorption spectra of wC-s-s-25, P25/wC-s-s-25, and wood block (from top to bottom), and (b) IR images of wC-s-s-25 in air (upper) and floating on water (lower) upon irradiation of simulated sunlight for 0, 1 and 5 min (from left to right).

temperature change at 1 sun, and the equilibrium temperature was as high as about 56.8 °C with irradiation for 5 min (Fig. 2b, lower). The phenomenon is attributed to the heterostructures of the partially carbonized wood, in which carbon components are served as a solar collector and wood components reduce heat loss. Hence, the completely carbonized wood block with a semi-spherical end (wC-c-s) showed low temperature after light irradiation due to high heat loss (Fig. S6a†). Solar-thermal conversion efficiency cannot be affected by P25 nanocrystals, and P25/wC-s-s-25 displayed a similar temperature change to wC-s-s-25 at 1 sun (Fig. S6b†). In contrast, a natural wood block with a semi-spherical end floating on water showed a low equilibrium temperature (~40.1 °C) upon 1 sun irradiation for ~5 min, which was mainly attributed to weak thermal conductivity and light absorption ability and low solar-thermal conversion efficiency of natural wood.

Solar water evaporation and RhB photo-degradation of RhB

Before the performance of our designed bifunctional evaporator P25/wC-s-s-25 for the purification of seawater that was taken from the Yellow Sea (coordination: E121.58, N38.90) was carefully examined, the wC-s-s-25 evaporator floated on the seawater (60 mL) filled in a 100 mL glass beaker, and the time-dependent water evaporation driven by solar energy upon the irradiation of simulated sunlight were performed. According to the amount of vaporized water plotted in Fig. 3a (black), the average solar water evaporation rate (r) of wC-s-s-25 was 1.02 kg m^{-2} h^{-1} at 1 sun within 1.5 h after the subtraction of the weight of water from the evaporation of seawater without any evaporators. It is noted that the cross-section area of wood carbon is used to calculate the rate. Solar-to-vapour energy efficiency (η_{th}), which is a key indicator to gauge the performance of solar water evaporation, is calculated according to the following eqn (1),

$$\eta_{th} = \frac{\dot{m}(h_s + h_{LV})}{I} \quad (1)$$

wherein $\dot{m}$ is the mass flux, h_s is the sensible heating, h_{LV} is the enthalpy of liquid–vapor phase change of water, and I is the intensity of incident light on the surface of the evaporator at 1 sun.[39,40] Hence, η_{th} of wC-s-s-25 is up to 72.1% based on eqn (1) (Fig. 3b). The wC-s-s-25 evaporator exhibits a similar solar water evaporation performance in the seawater in the presence of organic pollutant RhB; the solar water evaporation performance was not seriously affected by P25 nanocrystals based on the calculated r and η_{th} (Fig. S7†). Natural wood block shows an inferior solar water evaporation performance (r: 0.34 kg m^{-2} h^{-1}; η_{th}: 24.6%) possibly due to low solar energy harvesting ability (Fig. 3a and b). In addition to the intrinsic properties of photothermal materials, the structures of the materials can deeply influence their solar water evaporation performance. The flattened surface structures have a smaller surface area in terms of spherical surface structures if both blocks possess the same cross-section area, and thereby the wood block with two flat ends surficially carbonized at one end for 25 min (wC-f-s-25) shows lower solar water evaporation performance (r: 0.86 kg m^{-2} h^{-1}; η_{th}: 60.5%) compared to wC-s-s-25 (Fig. 3a and b). Given the high thermal conductivity of carbon leading to heat loss to bulk water and the environment, the completely carbonized wood blocks with a semi-spherical end (wC-c-s) show inferior solar water evaporation performance (r: 0.77 kg m^{-2} h^{-1}; η_{th}: 54.8%) (Fig. 3a and b) in terms of wC-s-s-25.

On this basis, we further discussed the effect of the thickness of carbonization layers, generally determined by carbonization time, and the thickness of surficially carbonized wood blocks on solar water desalination capability. Various photothermal materials of wC-s-s with different carbonization times exhibit different performances of solar water generation (Fig. S8a†). These results reveal that wC-s-s with too thin or too thick carbon layers are not favourable for solar water desalination. While the thickness of the carbon layer is ~0.6 cm (carbonization time: 25 min), the as-made wC-s-s-25 is considered as the best evaporator that enables the balance of solar energy harvesting and heat loss. In addition, if carbonization time is kept at 25 min, the photothermal materials of wC-s-s with different thicknesses (2, 2.5, and 3 cm) show slightly different solar water evaporation performance (Fig. S8b†).

Generally, water evaporation on the top carbon layer can induce a capillary force to continuously drive seawater to flow to the top layer for desalination; this would induce the formation of salt crystals on the carbon layers of the evaporator after irradiation for 24 h at 1 kW cm^{-2} (Fig. S9a†), causing the evaporation efficiency to decrease due to these salt crystals hindering light absorption of carbon. In our case, these salt crystals were easily removed from the surfaces of carbon layers when the evaporator with salt was kept in the seawater overnight (Fig. S9b†). Hence, wC-s-s can be considered as a self-regeneration solar evaporator that is allowed to reuse in desalination with the stable performance of solar water evaporation if the evaporator is alternately irradiated by simulated sunlight at 12 h intervals (Fig. S10†).

TiO_2 has been considered as a conventional photocatalyst for the degradation of organic pollutants based on its low cost in the preparation process and high stability of chemical/photo etching resistance.[41,42] P25 nanocrystals (5 mg) were dispersed in seawater (60 mL) containing RhB with a concentration of 1×10^{-5} M upon irradiation at 1 kW cm^{-2} for 1.5 h. Prior to photodegradation, the mixture was stirred in darkness for 1 h to eliminate the influence of the adsorption of RhB on the photocatalytic capability of P25 nanocrystals. Almost all RhB was removed according to absorbance change of RhB at 554 nm

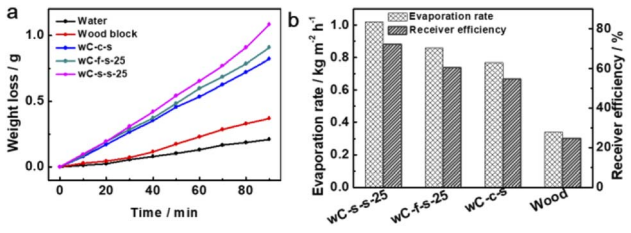

Fig. 3 Solar water generation performance of different schemes: (a) time-dependent evaporation water weight at 1 kW m^{-2}, and (b) evaporation rate and solar thermal receiver efficiency of different evaporators under irradiation at 1 kW m^{-2} for 90 min.

within 1 h (Fig. 4a). The contribution of photo-degradation to absorbance change is about 92% (Fig. 4e and f). After the subtraction of RhB degradation without introducing P25 nanocrystals (Fig. 4b), the photo-degradation efficiency of P25 against RhB is about 75% (Fig. 4f).[42] On this basis, bifunctional P25/wC-s-s-25 composites, including 5 mg of P25, were used for the study of photo-degradation against the RhB dye. Before light irradiation, a 100 mL glass beaker with a P25/wC-s-s-25 composite floated RhB solution (60 mL) was kept in the dark for 1 h to fully adsorb (~15.9%, Fig. 4e and f). Afterwards, the beaker was irradiated under simulated sunlight irradiation, and the photo-degradation efficiency against RhB was about 76% within 1.5 h according to the absorbance of RhB dyes at 554 nm (Fig. 4c). In contrast, if P25/wC-s-s-25 was replaced by wC-s-s-25, the photo-degradation efficiency against RhB dyes was decreased to 15.4% under otherwise identical conditions (Fig. 4d–f). The result reveals that the enhanced photo-degradation performance of P25/wC-s-s-25 is significantly dependent on P25 nanocrystals. In the photo-degradation process, to reduce the impact of water evaporation induced by the wC-s-s-25 evaporator on experimental results, water was added to the photo-degradation system according to the amount of water evaporated. In comparison with P25 powder, P25/wC-s-s-25 shows slightly lower photo-degradation performance within 1.5 h. The phenomenon is mainly due to the need for RhB dyes to diffuse to the vicinity of P25/wC-s-s-25 that allows producing free radicals, such as hydroxyl radical ($OH^{\bullet}$) and superoxide radical ($O_2^{\bullet -}$),[43,44] facilitating the transformation of RhB dyes to CO_2 and other oxidation products; thereby, if extending the irradiation time to 3 h, the RhB dye was completely degraded by P25/wC-s-s (Fig. S11†). To confirm the RhB dye degradation by $O_2^{\bullet}$ and $OH^{\bullet}$ radicals, when the scavenger of *tert*-butanol was added to the system, the degradation reaction of the RhB dye was inhibited (Fig. S12†).[45] The result reveals the possibility of the RhB dye being degraded by $O_2^{\bullet}$ and $OH^{\bullet}$ radicals.

To further explore its potential practical application in water treatment, the recyclability of bifunctional P25/wC-s-s-25 for solar water evaporation and dye degradation was examined. In detail, the composite was placed into a glass beaker containing RhB solution in seawater. The *r* of P25/wC-s-s-25 is still as high as ~0.96 kg m^{-2} h^{-1} at 1 sun after 6 runs of experiments (Fig. S13†). As for the photo-degradation of P25/wC-s-s-25, the reduced amount of RhB in the system decreases from ~92% to ~85%, which is mainly attributed to the decrease in the adsorption ability of P25/wC-s-s-25, and the photo-degradation efficiency of P25/wC-s-s-25 against RhB is still ~74% (Fig. S14†). In addition, natural sunlight was used as a light source to provide solar energy; thereby, the experimental equipment was placed outdoors (Dalian, China) for 10 h from 8:00 to 18:00 in August. The total amount of water evaporated is ~5.12 g (Fig. 5a). Owing to different irradiance intensities of natural sunlight at different times (Fig. S15†), different rates of water evaporation can be detected within 10 h at different time ranges (Fig. 5a), and the average *r* of P25/wC-s-s-25 is as high as 0.72 kg m^{-2} h^{-1} after the subtraction of the weight of water from the evaporation of seawater without any evaporators.

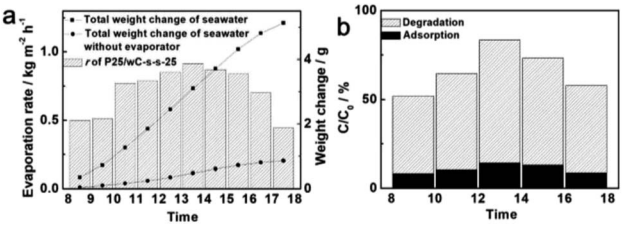

Fig. 5 (a) Time-dependent solar water generation performance of P25/wC-s-s-25 and (b) time-dependent photo-degradation of RhB dyes by P25/wC-s-s-25 after RhB adsorption under natural sunlight from 8:00 to 18:00.

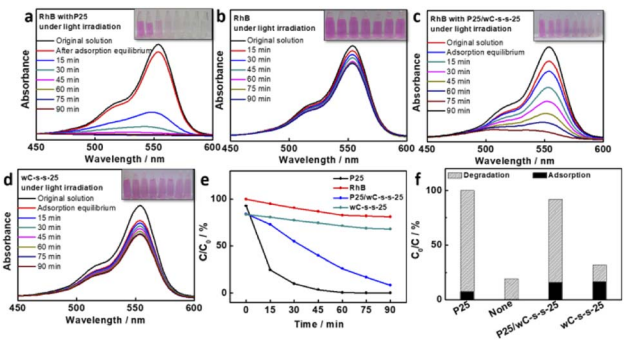

Fig. 4 UV-visible absorption spectra of RhB solution after adsorption and irradiation by simulated sunlight at different times in the presence of different materials: (a) P25, (b) none, (c) P25/wC-s-s-25 and (d) wC-s-s-25, (e) time-dependent photo-degradation of RhB dyes by different materials after subtraction of RhB adsorption, and (f) photo-degradation of RhB dyes within 1.5 h after RhB adsorption. Insets are optical images of the RhB solution.

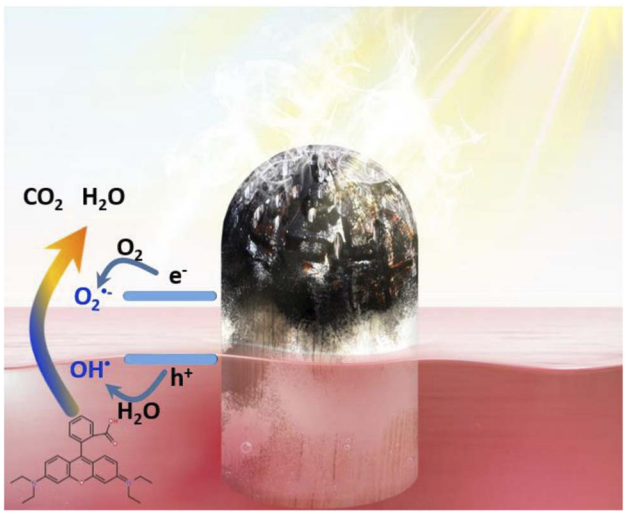

Fig. 6 Schematic diagrams of solar water generation and photo-gradation of RhB dyes using P25/wC-s-s-25 bifunctional materials. CB and VB represent the conduction band and valence band of P25, respectively.

Similarly, RhB dyes can also be degraded by natural sunlight; P25/wC-s-s-25 exhibits the highest photo-degradation efficiency against RhB dyes from 12:00 to 14:00 (Fig. 5b). P25/wC-s-s-25 as a bifunctional self-regeneration solar evaporator by the spontaneous removal of salt in seawater overnight shows the stable performance of solar water generation and RhB degradation for 10 days without any treatment.

The mechanism of the heterostructures of P25/wC-s-s-25 for solar water evaporation and photo-degradation of RhB is clearly revealed in Fig. 6. The semi-spherical carbon layers above the surfaces of seawater fully absorb solar energy that can be converted into thermal energy, driving water evaporation from aligned pores by capillary force. The light absorption of P25 nanocrystals loaded on the surfaces of the wood domain is almost not affected by carbon layers, and the P25 photocatalyst is excited to generate electrons and holes, leading to the formation of $O_2^{\bullet}$ and $OH^{\bullet}$ by reacting with O_2 and H_2O, respectively. Finally, RhB dyes are degraded by both $O_2^{\bullet}$ and $OH^{\bullet}$ radicals through an oxidation process.

Conclusions

In summary, we have successfully fabricated low-cost bio-based bifunctional water-purification materials of P25/wC-s-s-25 by tge surficial carbonization of wood blocks at the semi-spherical end and drop casting the surface of the wood zone with commercial P25 nanocrystals. The as-made P25/wC-s-s-25 exhibits bifunctional properties of solar water evaporation with 70.6% solar-to-vapour energy efficiency and photo-degradation of RhB dyes with 76% efficiency upon irradiation at 1 kW cm^{-2} for 1.5 h. The high performance is mainly attributed to (i) large surface area induced by porous structures and spherical structures, leading to the improvement of light absorption and water evaporation, and (ii) the separated heterostructures between P25 and carbon layers do not influence each other on light harvesting, maximizing solar energy collection by P25 and carbon. This research comes up with a simple strategy to produce cost-efficient water purification systems, in which not only clean and potable water can be obtained, but some organic pollutants can be degraded from the polluted seawater by natural sunlight, potentially addressing the issue of global freshwater shortage and environmental pollution.

Note that since the microstructures of the white oak are related to its origin and age, the different white oak could lead to the possibility of low reproducibility in solar water generation performance. Nonetheless, the important conclusion is that the carbonized wood blocks with spherical structures show higher solar water generation performance than the carbonized wood blocks with flattened structures.

Author contributions

Conceptualization: Liyong Chen, Zhizhi Gu, and Hui Zhang; methodology, visualization, and formal analysis: Hui Zhang, Yao Wang, and Xiaohua Wang; writing – original draft preparation: Zhizhi Gu and Hui Zhang; funding acquisition, supervision, writing – review & editing: Liyong Chen.

Conflicts of interest

The authors declare no competing financial interest.

Acknowledgements

The authors thank the financial support from the Natural Science Foundation of Anhui Province of China (Grant No. 2108085MB47), and the National Natural Science Foundation of China (Grant No. 21671030).

Notes and references

1 N. Ferronato and V. Torretta, *Int. J. Environ. Res. Public Health*, 2019, **16**, 1060.
2 J.-Q. Xiong, M. B. Kurade and B.-H. Jeon, *Trends Biotechnol.*, 2018, **36**, 30–44.
3 C. Li, C. Guo, V. Fitzpatrick, A. Ibrahim, M. J. Zwierstra, P. Hanna, A. Lechtig, A. Nazarian, S. J. Lin and D. L. Kaplan, *Nat. Rev. Mater.*, 2020, **5**, 61–81.
4 X. Ji, H. Wang, H. Wang, T. Zhao, Z. A. Page, N. M. Khashab and J. L. Sessler, *Angew. Chem., Int. Ed.*, 2020, **59**, 23402–23412.
5 K. E. Murray, S. M. Thomas and A. A. Bodour, *Environ. Pollut.*, 2010, **158**, 3462–3471.
6 H. Wang, X. Mi, Y. Li and S. Zhan, *Adv. Mater.*, 2020, **32**, 1806843.
7 M. Van den Bergh, A. Krajnc, S. Voorspoels, S. R. Tavares, S. Mullens, I. Beurroies, G. Maurin, G. Mali and D. E. De Vos, *Angew. Chem., Int. Ed.*, 2020, **59**, 14086–14090.
8 P. J. J. Alvarez, C. K. Chan, M. Elimelech, N. J. Halas and D. Villagan, *Nat. Nanotechnol.*, 2018, **13**, 634–641.
9 K. K. Khaing, D. Yin, Y. Ouyang, S. Xiao, B. Liu, L. Deng, L. Li, X. Guo, J. Wang, J. Liu and Y. Zhang, *Inorg. Chem.*, 2020, **59**, 6942–6952.
10 M. J. F. Calvete, G. Piccirillo, C. S. Vinagreiro and M. M. Pereira, *Coord. Chem. Rev.*, 2019, **395**, 63–85.
11 G. Rammohan and M. N. Nadagouda, *Curr. Org. Chem.*, 2013, **17**, 2338–2348.
12 C.-C. Wang, J.-R. Li, X.-L. Lv, Y.-Q. Zhang and G. Guo, *Energy Environ. Sci.*, 2014, **7**, 2831–2867.
13 M. Czaplicka, *J. Hazard. Mater.*, 2006, **134**, 45–59.
14 V. A. Sakkas, M. A. Islam, C. Stalikas and T. A. Albanis, *J. Hazard. Mater.*, 2010, **175**, 33–44.
15 P. Song, J. Cui, J. Di, D. Liu, M. Xu, B. Tang, Q. Zeng, J. Xiong, C. Wang, Q. He, L. Kang, J. Zhou, R. Duan, B. Chen, S. Guo, F. Liu, J. Shen and Z. Liu, *ACS Nano*, 2020, **14**, 595–602.
16 J. Mao, M. Ge, J. Huang, Y. Lai, C. Lin, K. Zhang, K. Meng and Y. Tang, *J. Mater. Chem. A*, 2017, **5**, 11873–11881.
17 J. Y. C. Lim, S. S. Goh, S. S. Liow, K. Xue and X. J. Loh, *J. Mater. Chem. A*, 2019, **7**, 18759–18791.
18 R.-P. Ren, W. Li and Y.-K. Lv, *J. Colloid Interface Sci.*, 2017, **500**, 63–68.
19 N. Liu, L. Hao, B. Zhang, R. Niu, J. Gong and T. Tang, *Energy Environ. Mater.*, 2021, **5**, 617–626.
20 P. Tao, G. Ni, C. Song, W. Shang, J. Wu, J. Zhu, G. Chen and T. Deng, *Nat. Energy*, 2018, **3**, 1031–1041.

21 L. Jauffred, A. Samadi, H. Klingberg, P. M. Bendix and L. B. Oddershede, *Chem. Rev.*, 2019, **119**, 8087–8130.
22 M. Gao, L. Zhu, C. K. Peh and G. W. Ho, *Energy Environ. Sci.*, 2019, **12**, 841–864.
23 H. A. Atwater and A. Polman, *Nat. Mater.*, 2010, **9**, 205–213.
24 Y. Wang, L. Zhang and P. Wang, *ACS Sustainable Chem. Eng.*, 2016, **4**, 1223–1230.
25 L. Zhu, M. Gao, C. K. N. Peh, X. Wang and G. W. Ho, *Adv. Energy Mater.*, 2018, **8**, 1702149.
26 Y. Shao, Z. Jiang, Y. Zhang, T. Wang, P. Zhao, Z. Zhang, J. Yuan and H. Wang, *ACS Nano*, 2018, **12**, 11704–11710.
27 C. Jia, Y. Li, Z. Yang, G. Chen, Y. Yao, F. Jiang, Y. Kuang, G. Pastel, H. Xie, B. Yang, S. Das and L. Hu, *Joule*, 2017, **1**, 588–599.
28 T. Li, H. Liu, X. Zhao, G. Chen, J. Dai, G. Pastel, C. Jia, C. Chen, E. Hitz, D. Siddhartha, R. Yang and L. Hu, *Adv. Funct. Mater.*, 2018, **28**, 1707134.
29 Z. Chen, B. Dang, X. Luo, W. Li, J. Li, H. Yu, S. Liu and S. Li, *ACS Appl. Mater. Interfaces*, 2021, **13**, 2115.
30 X. Chen, X. Zhu, S. He, L. Hu and Z. J. Ren, *Adv. Mater.*, 2020, **33**, e2001240.
31 Q.-F. Guan, Z.-M. Han, Z.-C. Ling, H.-B. Yang and S.-H. Yu, *Nano Lett.*, 2020, **20**, 5699–5704.
32 M. Zhu, Y. Li, G. Chen, F. Jiang, Z. Yang, X. Luo, Y. Wang, S. D. Lacey, J. Dai, C. Wang, C. Jia, J. Wan, Y. Yao, A. Gong, B. Yang, Z. Yu, S. Das and L. Hu, *Adv. Mater.*, 2017, **29**, 1704107.
33 X.-D. Zhu, Y.-J. Wang, R.-J. Sun and D.-M. Zhou, *Chemosphere*, 2013, **92**, 925–932.
34 J. Yu and J. Ran, *Energy Environ. Sci.*, 2011, **4**, 1364–1371.
35 J. Zhang, Z. Xiong and X. S. Zhao, *J. Mater. Chem.*, 2011, **21**, 3634–3640.
36 V. Swamy, *Phys. Rev. B: Condens. Matter Mater. Phys.*, 2008, **77**, 195414.
37 H. L. Ma, J. Y. Yang, Y. Dai, Y. B. Zhang, B. Lu and G. H. Ma, *Appl. Surf. Sci.*, 2007, **253**, 7497–7500.
38 H. A. Atwater and A. Polman, *Nat. Mater.*, 2010, **9**, 205–213.
39 H. Ghasemi, G. Ni, A. M. Marconnet, J. Loomis, S. Yerci, N. Miljkovic and G. Chen, *Nat. Commun.*, 2014, **5**, 4449.
40 X. Wang, Y. He, X. Liu, G. Cheng and J. Zhu, *Appl. Energy*, 2017, **195**, 414–425.
41 I. K. Konstantinou and T. A. Albanis, *Appl. Catal., B*, 2004, **49**, 1–14.
42 J. Schneider, M. Matsuoka, M. Takeuchi, J. Zhang, Y. Horiuchi, M. Anpo and D. W. Bahnemann, *Chem. Rev.*, 2014, **114**, 9919–9986.
43 Y.-H. Chiu, T.-F. M. Chang, C.-Y. Chen, M. Sone and Y.-J. Hsu, *Catalysts*, 2019, **9**, 430.
44 M. A. Rauf, M. A. Meetani and S. Hisaindee, *Desalination*, 2011, **276**, 13–27.
45 L. Wang, X. Lan, W. Peng and Z. Wang, *J. Hazard. Mater.*, 2021, **408**, 124436.